scientific reports

Check for updates

OPEN

Observation of temporal optical solitons in a topological waveguide

Ju Won Choi[1], Byoung-Uk Sohn[1], Hongwei Gao[1], George F. R. Chen[1], Jia Sheng Goh[2], Doris K. T. Ng[2] & Dawn T. H. Tan[1,2]✉

Photonic topological systems may be exploited in topological quantum light generation, the development of topological lasers, the implementation of photonic routing systems and optical parametric amplification. Here, we leverage the strong light confinement of an ultra-silicon-rich nitride (USRN) topological waveguide adopting the 1D Su-Schrieffer-Heeger (SSH) system with a topological domain wall. We present the formation and propagation of temporal optical solitons in the topological waveguide, exhibiting two-fold temporal compression. We further observe a saturation in the output power at sufficiently high input powers. It is further observed that pulse propagation through a trivial, non-topological waveguide does not lead to similar temporal soliton dynamics. The demonstrated topological system allows for the temporal compression to be manipulated through power tuning via topological control of delocalization of the topological mode. This design degree of freedom allows temporal solitons to be generated in a topological waveguide while providing straightforward control of temporal pulses in practical applications.

The link between condensed matter physics and photonics was significantly strengthened when researchers proposed the photonic equivalent of the Quantum Hall effect. This seminal report from Haldane and Raghu theoretically predicted that time-reversal symmetry breaking for light could be achieved using magneto-optic materials, thus enabling unidirectional propagation[1]. Haldane and Raghu's theoretical prediction was reduced to practice shortly after by Z. Wang et al., who reported the first demonstration of a topological photonic crystal implemented on Yttrium-iron-garnet[2]. Magnet-optic materials are akin to non-reciprocal media, providing the ability for time-reversal symmetry to be broken. Dielectric systems on the other hand, have advantages such as ease of fabrication and availability, and potential compatibility with CMOS processes which make them more suited for large-scale manufacturability. In all-dielectric systems, only effective time-reversal symmetry breaking can be achieved since reciprocity is conserved[3]. Nonetheless, their considerably easier implementation has fuelled extensive development. Advances in topological photonics have recently exhibited substantial potential across diverse applications, many of which involve all-dielectric systems. Some recent advancements include topological quantum light generation[4,5], the development of topological lasers[6,7], and the implementation of photonic routing systems[8–10].

The discovery of topological solitons, widely recognized as being first observed in the Su-Schrieffer-Heeger (SSH) system, marked a significant breakthrough in condensed matter physics, similar to the anomalous Hall conductance observed in periodic systems[11,12]. In photonics, topological waveguides utilize the zero modes created at the interface between two distinct topological domains within dimerized lattices. In the 1D SSH model, each unit cell comprises two sites, and the system's topology is dictated by the relative strengths of the intracell coupling (v) and the intercell coupling (w). The boundary separating regions with different topological properties represents a topological domain wall, which gives rise to a topological mode, characterized as having its peak coincident with the boundary between the two regions[13].

Nonlinear phenomena have been theoretically studied in a variety of topological systems. Of note, Ref. 12 reported topological edge states and topological gap solitons residing in the same bandgap in the nonlinear Dirac model. Nonlinear switching between trivial and nontrivial states in a Floquet lattice of coupled waveguides was demonstrated[14]. Observations of optical spatial solitons in a photonic Floquet topological insulator revealed that a lattice with non-zero Floquet winding number working with optical nonlinearities could induce solitons residing in topological gaps[15]. Most recently, it was theoretically predicted that a topological ring resonator could provide a new avenue for the generation of frequency combs[16].

The topology of a system confers unique optical properties to propagating light. On the other hand, the material on which the topological system is implemented serves as a vessel for light matter interaction of varying degrees. Ultra-silicon-rich nitride (USRN) is a CMOS (complementary metal-oxide semiconductor)-compatible

[1]Photonics Devices and System Group, Singapore University of Technology and Design, 8 Somapah Rd, Singapore 487372, Singapore. [2]Institute of Microelectronics (IME), Agency for Science, Technology and Research (A*STAR), 2 Fusionopolis Way, Innovis #08-02, Singapore 138634, Singapore. ✉email: dawn_tan@sutd.edu.sg

platform with a high Kerr nonlinearity of $n_2 = 2.8 \times 10^{-13}$ cm^2/W and negligible nonlinear loss near the 1550 nm wavelength[17–19] which has been used for much success in the observation of soliton phenomena including pure-quartic Bragg solitons[20], gap solitons[21], soliton fission[22], and high-order soliton-effect temporal compression[23]. These have been observed in both on-chip Bragg gratings and photonic waveguides, largely facilitated by the large dynamic range of dispersive and nonlinear properties which may be engineered in USRN devices. Previous work show that various types of optical solitons may be efficiently generated in the USRN platform which is CMOS-compatible, enabling ease of integration with CMOS electronics. Most recently, efficient optical parametric amplification leveraging the strong light localization in a topological SSH waveguide with a domain wall was demonstrated[13]. It was further elucidated that the Kerr effect could induce a delocalization on the topological mode. Observations of the strong interaction of the topological mode with the medium seeded further investigations into nonlinear optical phenomena implemented using the SSH model.

In this paper, we investigate soliton formation in a topological structure implemented on USRN, leveraging both the unique light localization properties availed by topology and the high Kerr nonlinearity in USRN. Compared to photonic waveguides, the optical confinement can be manipulated using the gaps between waveguides in the topological SSH model, which can result in the control of optical losses impacting optical soliton generation. This unique feature avails a new design degree of freedom to the SSH model not available in conventional waveguides. The temporal compression based on high-order solitons may further be used in applications such as temporal manipulation of optical pulses by power. Consequently, high-order solitons in topological waveguides may be used for the robust tuning of temporal optical pulses. We report observations of optical temporal solitons propagating within a boundary waveguide of the USRN topological waveguide. A dimerized coupled waveguide system with two bands, each with different Zak phase, and a boundary waveguide provide topological localization of the mode. Topological light guiding and nonlinear interaction with the propagating medium lead to experimental observations of 2× temporal compression at a peak power of 45.3 W. In addition, output power saturation of the input power exists at the boundary waveguide for input pulses < 1ps. Simulations including the reduced power factor using the nonlinear Schrödinger equation were performed to explain the temporal soliton behavior. Theoretical simulations reveal similar extents of temporal compression factor as the experiment. Lastly, experiments using a trivial, non-topological waveguide array reveal no temporal compression, indicating that the observed topologically guided temporal soliton behaviour is a result of topological localization.

Results

Theoretical description of the temporal evolution of light in the USRN topological waveguide

We solve the equation to investigate the temporal behaviour. Our experimental condition is that the input is launched into the defect waveguide and output from the defect waveguide is measured. The input field into the defect waveguide is not exact boundary mode and the spatial amplitude for each waveguide is modulated as below Fig. 1 (blue line is for central (boundary) waveguide, red line is for nearest waveguide and green line is for next neighbour) but the amplitude flattens after some extent of propagation through the waveguide. We utilize the flattened amplitude as the combination of the boundary mode with reduced peak amplitude as depicted in Fig. 1c,f. The extent of amplitude reduction will change when the input peak power increases because the Kerr effect modifies the shape of the boundary mode[13]. Thus, we can solve for the temporal distribution at the boundary waveguide by assuming that effectively, the modal distribution is that of the boundary mode and the peak power is reduced to $P_{in}\eta\ (P_{in})$ depending on input peak power. Here, P_{in} is the input peak power and $\eta\ (P_{in})$ is the reduced power factor which varies as a function of P_{in}.

The nonlinear Schrödinger equation (NLSE) governing propagation of optical pulses in spatial coupled waveguides with SSH distribution is used for numerical calculations. The input optical field from the central waveguide may excite not only the dominant topological boundary mode but also bulk modes. The topological boundary mode is modified by the nonlinear Kerr effect with a reduced amplitude at the boundary waveguide[13]. In the simulation, $P_{\text{in}}{}^{*}\eta(P_{\text{in}})$ is applied to input power in the NLSE simulation to investigate the temporal propagation of optical pulses at the boundary waveguide which explains the composition of the boundary modes in the real SSH waveguide system.

We use a variable decomposition method, decomposed to a spatial and a temporal part, to solve Maxwell's equations. The spatial mode for the SSH system with topological boundary consists of the boundary mode and two split bulk modes. We assume that the spatial boundary mode is excited dominantly and the bulk modes are excited with the very weak scale, therefore, the small excited bulk modes are superposed to propagate like a random basis at the coupled array waveguide. The oscillating amplitudes in Fig. 1c (low power) and Fig. 1f (high power) show the small excited bulk states (red and green lines) but the oscillating phenomena is reduced to almost zero because the more bulks states are superposed by the very devious phases. Therefore, the finally output amplitudes are the same as the boundary mode shape as shown in Fig. 1b (low power) and Fig. 1d (high power). Thus, the dominant boundary mode is assumed to propagate with the spatial shape, and it is confirmed that we can adopt the temporal nonlinear Schrödinger equation, Eq. (1) to analyse the temporal soliton phenomena.

For the topological invariant of the SSH, Zak phase, $\oint \langle u_k \left| \frac{\partial}{\partial k} \right| u_k \rangle \, dk$, is used. The dimerized SSH system is constructed with a boundary separating two regions of distinct bulk topology. The upper band exhibits a topological constant of $-\pi$, while the lower band has a topological constant of π [13]. This configuration results in the emergence of a single topological boundary state, which is a consequence of the disparity between the two bulk topological constants. We added the topological Zak phase in the Fig. 1a.

Input pulses enter the boundary waveguide and exit through the same waveguide, experiencing the variation of the reduced power factor ($\eta\ (P_{in})$) depending on the peak power. Therefore, the single waveguide with the reduced power factor can be exploited to explain this work. The NLSE to explain the temporal solitons at the boundary waveguide is shown as the following[24].

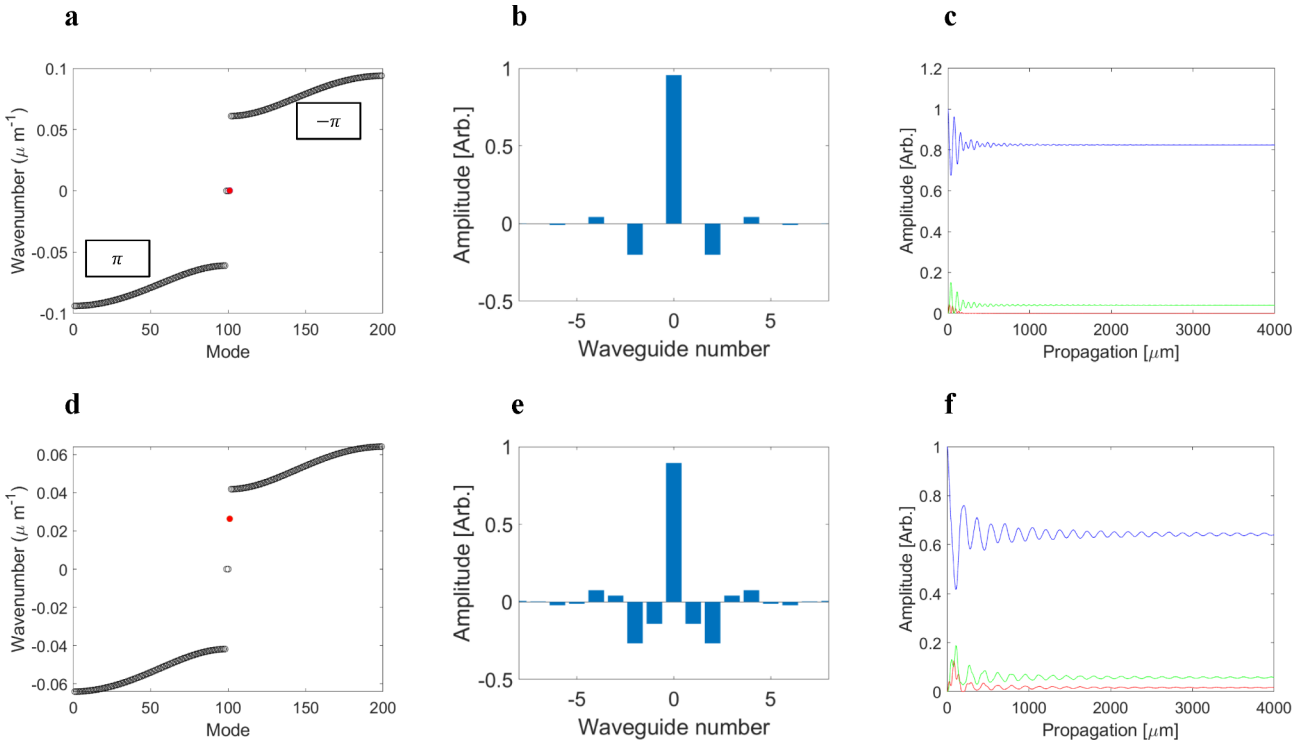

Fig. 1. (**a**) Energy band, (**b**) the mode shape for the boundary state (red dot) in Fig. 1**a**, and **(c)** spatial amplitude evolution for the center waveguide input at low peak power. (**d**) Energy band, (**e**) the mode shape for the boundary state (red dot) in Fig. 1**d** and (**f**) spatial amplitude evolution at high peak power; The red circle in the energy band corresponds to the topological boundary mode. For the amplitude propagation, the blue line represents the central waveguide (domain wall), the red line is for nearest neighbour waveguide and the green line is for next neighbour waveguide.

$$\frac{\partial A}{\partial z} = -\frac{\alpha}{2}A - i\frac{\beta_2}{2}\frac{\partial^2 A}{\partial t^2} + \frac{\beta_3}{6}\frac{\partial^3 A}{\partial t^3} + i\frac{\beta_4}{24}\frac{\partial^4 A}{\partial t^4} + i\gamma|A|^2 A \tag{1}$$

α represents the propagation loss coefficient of the boundary waveguide. A denotes the slowly varying envelope. The variables z and t correspond to the propagation and temporal coordinates, respectively. Additionally, β_2, β_3 and β_4 signify the group velocity dispersion (GVD), third-order dispersion (TOD), and fourth-order dispersion (FOD) coefficients, respectively.

The schematic of the SSH structure and the theoretically calculated temporal evolution of optical pulses

The topological photonic waveguide using USRN is designed as a dimerized coupled waveguide system based on the SSH model with a domain wall[13,25]. The gap between the waveguides G_w is designed to be narrower than G_v as the topology is considered non-trivial when strength of the intercell coupling (w) is stronger than that of the intracell coupling (v). The system was already demonstrated and proved to achieve good linear transmission properties and efficient nonlinear parametric amplification due to strong light localization. Figure 2a shows the device schematic of the topological waveguide with a domain wall (boundary waveguide) located at the center. Within our design, we employ 199 waveguides to guarantee a suitably expansive transverse dimension in the topological system concerning the localized boundary mode, which encompasses 9 waveguides. The single input waveguide is not identical to the topological boundary mode in the SSH waveguide. The bulk modes are excited and modulated; The modulated signal in turn spreads and undergoes an amplitude reduction according to propagation length. If the number of waveguides in the array is too small, the modulated signal will return to the boundary waveguide from the edge of the array. Now, the amplitude on the boundary waveguide is calculated at a finite number of waveguides. For our device length of 4 mm, the modulation almost vanishes when 199 waveguides are within the array. The cross-section of each waveguide is 600 nm (W) x 340 nm (H). G_w and G_v are designed to be 0.15 and 0.25 µm for the optimization of strong localization with coupling ratio, $v/w = 0.17$[13]. The device length is 4 mm, which is 20 times longer than the coupling length of 200 µm for the long gap, which is necessary to experience sufficient couplings between waveguides in the propagation and facilitates sufficient nonlinear interaction.

It was previously reported that for input pulses of ≤ 1 ps, the saturation of the output power in the boundary waveguide occurred with increasing input power, whereas the output power at the next neighbor waveguide increased with input power. This phenomenon was established to originate from the ability of Kerr nonlinear

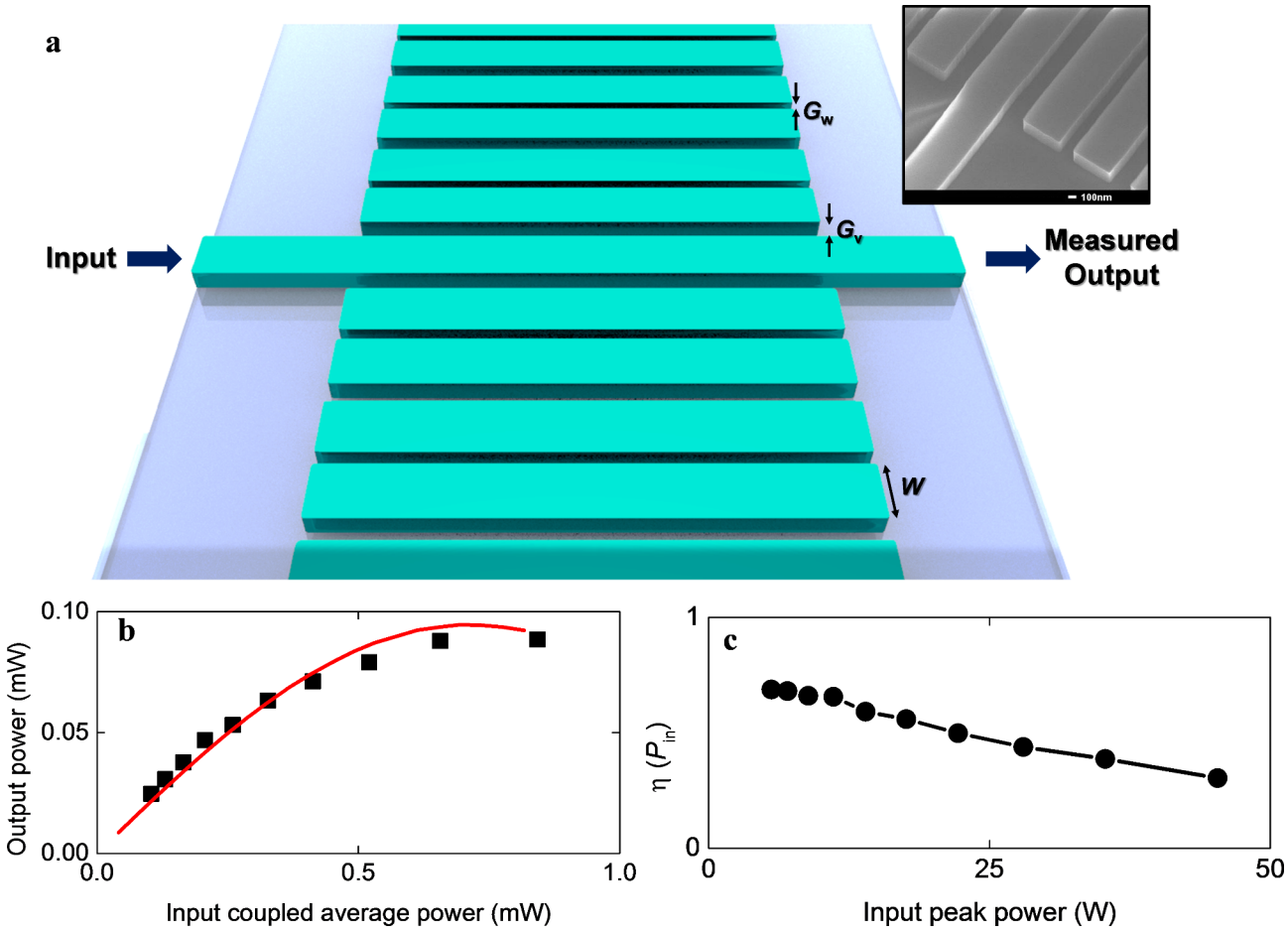

Fig. 2. (**a**) The schematic of the topological waveguide with a domain wall (The light comes in and out at the center waveguide called a domain wall). $W = 600$ nm is the width of USRN waveguides. The gap between the waveguides, $G_w = 0.15$ μm for the narrower gap and $G_v = 0.25$ μm for the wider gap. The inset shows a scanning electron micrograph of the topological waveguide where the scale bar corresponds to a length of 100 nm. (**b**) Measured output power as a function of input coupled average power. The red line depicts theoretical calculation using the nonlinear Schrödinger equation. (**c**) Reduced power factor (η) as a function of input coupled peak power.

effect to control the degree of localization of the topological mode by effectively breaking the chiral symmetry in the waveguide lattice. Nonlinear Kerr perturbation at the boundary is induced because the peak power of 1 ps is large enough to go over the forbidden band barrier[13]. Therefore, in this work, 0.93 ps input pulses are used to observe the temporal soliton in which the topological mode can be controlled with input power. The output average power after the device is measured as a function of input coupled average power, and shows the output power (Fig. 2b). As the propagation loss of the SSH structure itself exists with the fixed value along the propagation, the reduced power factor ($\eta\ (P_{in})$) is shown to decrease as input power increases as shown in Fig. 2c. ($\eta = 1$ means that there is no reduction in amplitude during the first propagation.) The characterized output power agrees well with theory as shown in Fig. 1, showing power-dependent η.

Figure 3a,b show the calculated second (β_2), third (β_3) and fourth order (β_4) dispersion. The refractive index of the USRN film is obtained experimentally using FTIR. The effective index (n_{eff}) of the structure is calculated using fully vectorial mode calculation (COMSOL) and allows us to derive GVD ($\beta_2 = \frac{\lambda^3}{2\pi c^2} \cdot \frac{d^2 n_{\mathrm{eff}}}{d\lambda^2}$), TOD ($\beta_3 = \frac{\partial \beta_2}{\partial \omega}$) and FOD ($\beta_4 = \frac{\partial^2 \beta_2}{\partial \omega^2}$), where c is the speed of light, λ is the wavelength, and ω is the angular frequency.

High-order solitons are described by the soliton number (N), defined as $N^2 = L_d/L_{nl}$, where L_d and L_{nl} are the dispersion and nonlinear lengths, respectively. Stronger temporal compression can be generated for larger soliton numbers when the propagation length coincides with the soliton evolution where the maximum temporal compression is achieved. For $N \geq 10$, it undergoes initial temporal compression, reducing to a fraction of its original pulse width due to the high-order soliton effect, even in cases where the propagation length does not match $z_{opt} = 1.6 z_0/N$, where $z_0 = \pi L_d/2$ is soliton period. Figure 3c,d show the temporal evolutions of pulses for the lowest ($P_{in} = 5.58$ W) and highest peak powers ($P_{in} = 45.3$ W) where the propagation length is $< z_{opt}$[24–26].

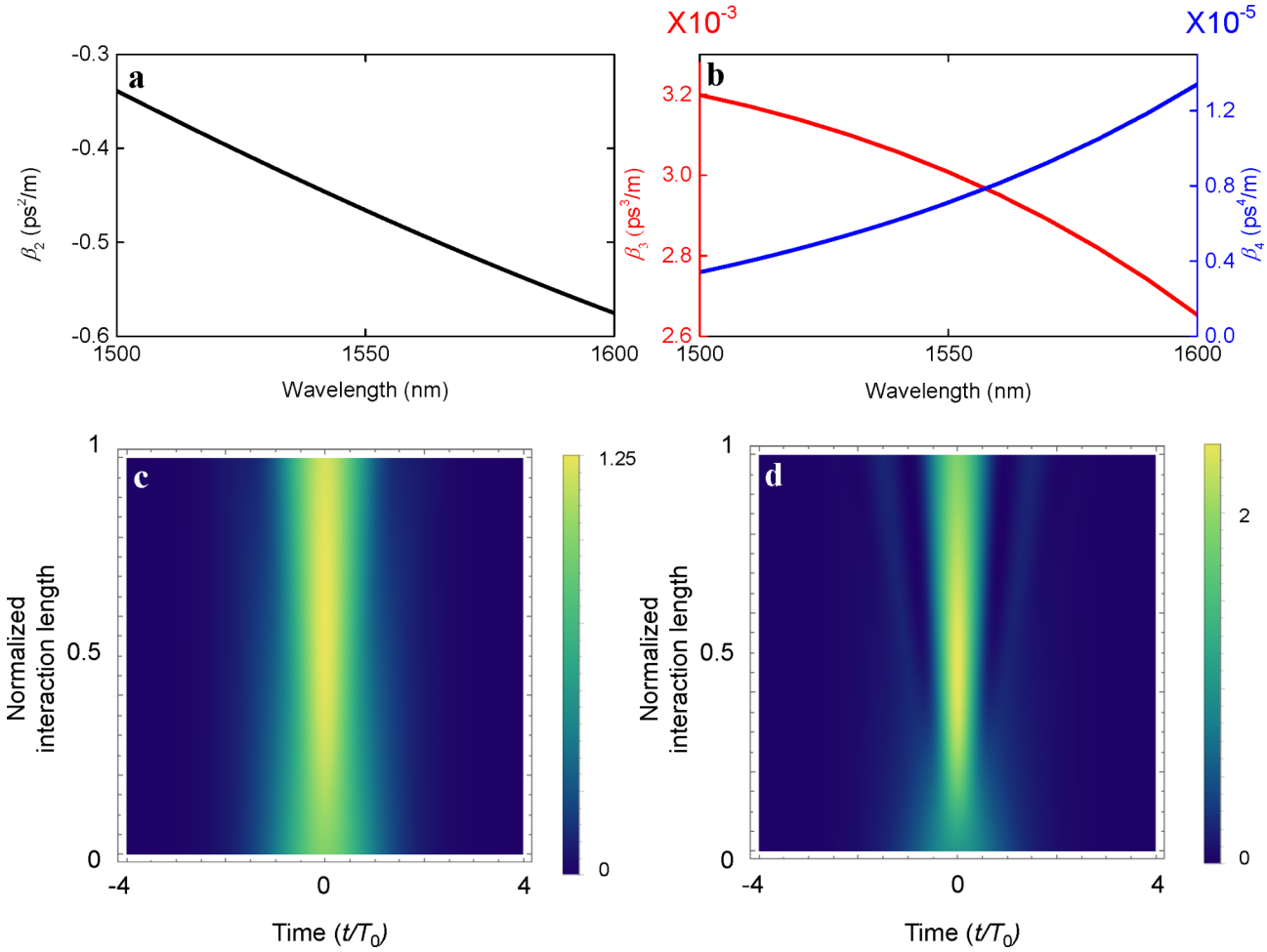

Fig. 3. (**a**) GVD, (**b**) TOD (red line) and FOD (blue line) at a wavelength of 1550.1 nm, used in the numerical modelling of the SSH device. (**c**) and (**d**) are the evolution of temporal traces for the peak power of the lowest (5.58 W) and the highest (45.3 W) along propagation, respectively. $T_0 = T_{FHWM\_}/1.76$ (for sech^2 pulse), where $T_{FHWM\_}$ is the input FWHM of 0.93ps.

The more temporally compressed pulses are generated along the propagation for P_{in}= 45.3 W ($N \sim 51$) in Fig. 3d compared to the temporal pulses for P_{in}= 5.58 W in Fig. 3c due to the higher-order soliton.

Experimental observations of temporal solitons in the USRN topological waveguide

To investigate the dynamics of pulse compression, a 0.93ps pulsed laser operating at a repetition rate of 20 MHz at a central wavelength of 1550.1 nm is utilized. The input optical pulses with fundamental TE-polarization are coupled into the SSH boundary waveguide using a tapered lensed fiber. Temporal profiles of the output pulses are measured using an autocorrelator. Figure 4a shows the experimental output temporal traces after applying the deconvolution factor (1.54 for sech^2 pulse) to autocorrelation traces. Even though the experimental and theoretical temporal traces are not exactly compared, the pulse width of both can be compared. The theoretical temporal traces from NLSE are shown in Fig. 4b. Theoretical and experimental temporal full width at half maximum (FWHM) are compared as shown in Fig. 4c. Both follow the same trends and there is good agreement between the theoretical and experimental values. The narrowest temporal width in the experiment is almost the same as the theoretical value for P_{in}=45.3 W. In the experiment, the narrowest temporal pulse width is 0.47ps indicating the compression factor of 1.98 as shown in Fig. 4d. This also shows that the NLSE including the reduced power factor can well describe the behavior of temporal solitons in an SSH boundary waveguide. The variations in the input peak power if the pulse induce a change in the refractive index of the boundary waveguide through a contribution from the nonlinear refractive index ($n_2.I$, where I is the intensity of the incident pulse), inducing varying extents of delocalization in the topological mode.

Temporal characterization of optical pulses propagating in a trivial (non-topological) waveguide

We observed soliton-effect temporal compression and output power saturation induced by the topological properties of the SSH waveguide with a domain wall. To confirm that these effects originated from topological properties at the boundary waveguide, we observed the same experiment using the trivial (non-topological)

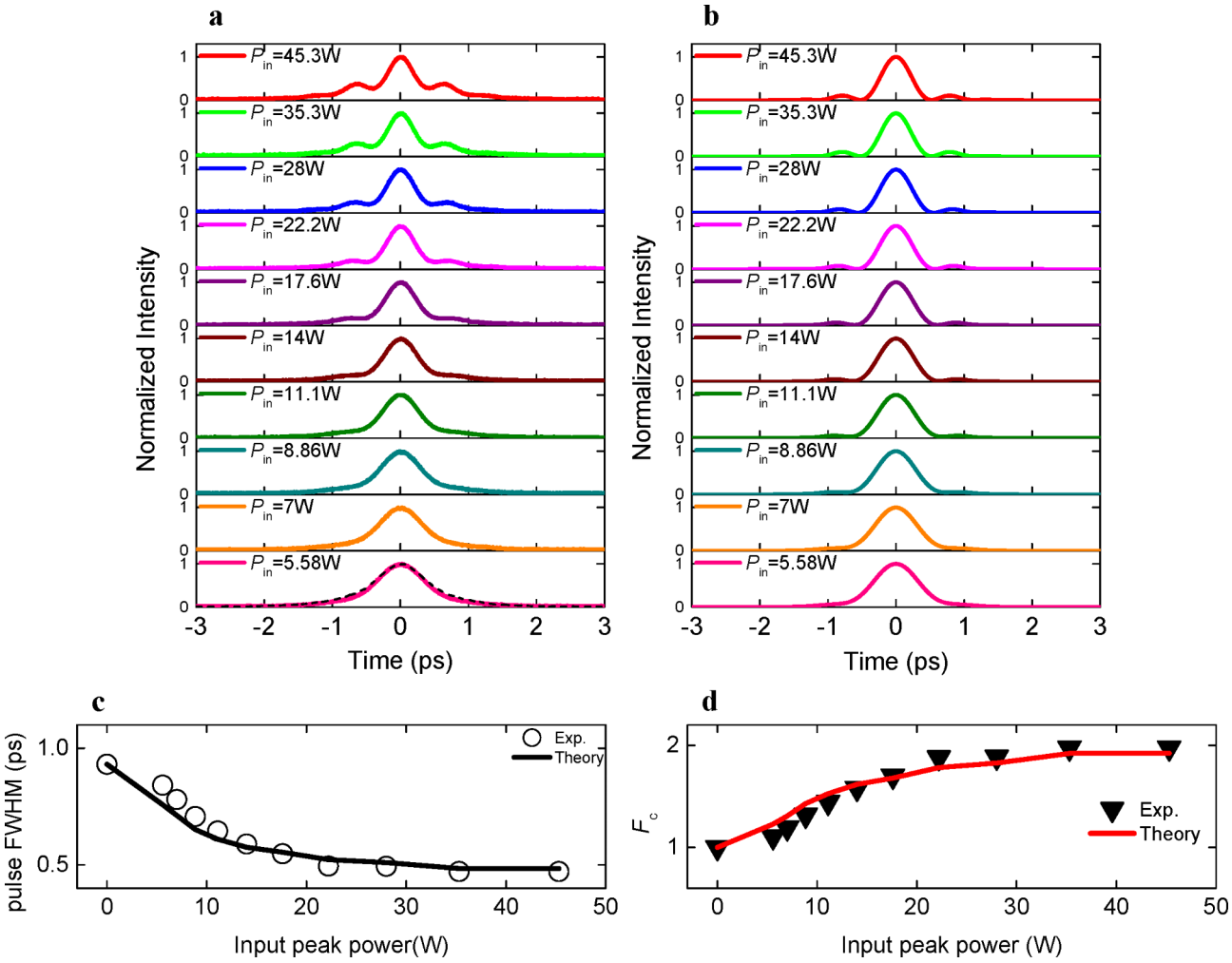

Fig. 4. (**a**) Experimental and (**b**) theoretical temporal traces at the output as a function of peak power. Experimental traces are obtained by applying the deconvolution factor on the autocorrelation traces to compare the pulse FWHM between the theoretical and experimental ones. The black dashed line in Fig. 3**a** depicts the input pulse. (**c**) Experimental pulse FWHM (empty circles) are compared with the theoretical ones (black line) on peak power. (**d**) The compression factor (F_c) of experimental (black triangles) and theoretical (red line) are compared as a function of peak power.

waveguide possessing the fixed gap of 0.25 μm between the waveguides in the array, leading to non-localization of light in the boundary waveguide. The same condition of input pulses is applied to the central waveguide. In the trivial waveguide where all elements are equidistant from one another, light is not localized to the boundary waveguide, but evanescently spreads away from the input, akin to spatial diffraction. Consequently, low output power is measured which results in high insertion loss. As may be observed in Fig. 5a, the linear output power as a function of input reflects a high, constant insertion loss. We further perform short pulse experiments with the trivial waveguide using the 0.93ps pulses. The output temporal trace is observed to have the same width as the input one showing there is no temporal compression induced by nonlinear soliton effect as shown in Fig. 5b. Comparing the topological and trivial waveguides, it is evident that the observed soliton formation and compression occurs only in the topological waveguide, induced by the topological light localization and associated nonlinear interaction. As a result of the topological light localization, pulses coupled into the device interact with the nonlinearity inherent in the material, thus undergoing self-phase modulation and encountering anomalous dispersion leading to temporal soliton formation. In the absence of the topological localization as in the trivial waveguide, light does not propagate confined to the boundary waveguide and the high insertion loss that results leads to marginal nonlinear interactions of the coupled light. We note further that the transmitted optical power is significantly lower in the trivial waveguide compared to the topological waveguide, since the lack of topological localization leads to the input pulses essentially spatially diffracting across the waveguide array.

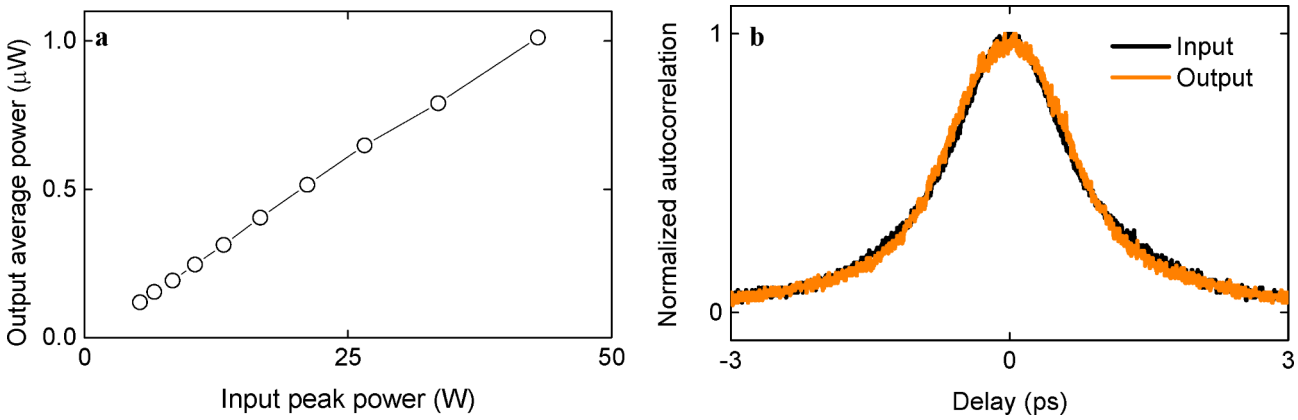

Fig. 5. Nonlinear optical properties of non-topological waveguide. (**a**) Measured output average power as a function of input peak power. (**b**) Experimental autocorrelation trace at the output (orange line), which is compared to the input autocorrelation trace (black line).

Discussion

Topological localization enables light to be localized at the boundary. The system studied here exhibits anomalous dispersion. Therefore, combined with the anomalous GVD and high Kerr nonlinearity, soliton compression can be implemented. This work shows that SSH waveguides with a domain wall may support the formation of optical solitons, as well as temporal compression through the associated soliton effects.

The interplay between topology and nonlinearity provides a rich platform for exploring novel optical phenomena and engineering unique photonic devices. Nonlinear effects leveraging topological photonics systems have been observed in a variety of platforms, including waveguides[27,28], photonic crystals[29], microcavities[30], atomic gases[31] and metamaterials[32]. Waveguide arrays have previously been used for topological photonics in the study of nonlinear effects[33]. As the topological dynamics are determined by the ratio of the nonlinear and linear coupling coefficients, topological nonlinear effects in waveguide arrays have previously been demonstrated in AlGaAs[27], lithium niobate[34], photorefractive waveguides[35] and fused silica glass[28].

Nonlinear extensions of linear topological models give rise to unique mechanisms for localizing the field, resulting in phenomena such as topological gap solitons[36], nonlinear edge states (both bulk and edge solitons)[37], embedded solitons[38], and semi-vortex solitons[39]. The formation of topological solitons can be explained by the local impact of nonlinearity inducing a domain wall between different topological phases, with the soliton being self-trapped by the interface.

In contrast to nonlinear effects in other topological systems[13–16], this work focuses on how the topological modes change and influence temporal soliton dynamics. By implementing local, on-site Kerr nonlinearities in a 1D SSH model with a domain wall using the CMOS-compatible USRN photonic platform, the generated solitons may be shown to enable tunability of temporal properties similar to solitons formed in conventional photonic waveguides, even though they are formed in a topological structure. Whereas other topological solitons focus on the trapping and localization of light, our results reveal the tunability of temporal shapes while having topological light confinement. In addition, the topological solitons demonstrated here are generated by interacting with the variable spatial modes, a fundamentally different mechanism from optical solitons in conventional photonic waveguides where the spatial modes are invariant. This approach facilitates a wide dynamic range of light control using nonlinear effects even though complicated interactions exist between the temporal and spatial domains. Our work showcases a new paradigm with which to control the temporal profile of a pulse by inducing varying degrees of delocalization in the topological mode through variations in the optical intensity.

In summary, we have experimentally demonstrated temporal optical solitons in a Su-Schrieffer -Heeger waveguide showing 2-fold temporal compression. We further observe output power saturation as the input power increases for < 1ps input pulses. The typical NLSE can be applied to explain the temporal soliton behavior at the boundary waveguides of the SSH structure by introducing the reduced power factor. The theoretical and experimental temporal widths as a function of input peak power exhibit a similar trend. For the maximum peak power of 45.3 W, the temporal pulse width is measured to be 0.47 ps, corresponding to 1.98 times temporal compression of 0.93 ps input pulses, showcasing soliton compression in a system which harnesses optical nonlinearity and topology. The generation of nonlinear soliton effects in the reported topological structure could facilitate new applications in topological pulse shaping and topological soliton lasers in the future.

Methods

Numerical calculations

The concept originates from tight binding theory, where the molecule's electronic states can be described by combination of the electronic states in a single atom.

Analogous to this, the N coupled waveguides can be described by the combination of modes in a single waveguide:

$$E(r,\omega) = F(x,y)\,\widetilde{A}(z,\omega)\exp(i\beta_0 z)$$

where $\widetilde{A}(z,\omega)$ is slow varying N-vector function of z, $F(x,y)$ is a mode in a single waveguide and β_0 is the fast wavenumber in the fast-varying term. From Maxwells wave equation, the two equations are derived[24]:

$$\frac{\partial^2 F}{\partial x^2} + \frac{\partial^2 F}{\partial y^2} + \left[\varepsilon(x,y,\omega)\,k_0^2 - \tilde{\beta}^2\right] F = 0$$

$$\frac{2i\beta_0 \partial\,\widetilde{A}}{\partial\, z} + \left(\widetilde{\beta}^{\,2} - \beta_0^{\,2}\right)\widetilde{A} = 0$$

Here, F is the eigenfunction, $\widetilde{\beta}$ is the eigenvalue and $\varepsilon(x,y,\omega)$ is the transverse distribution of the dielectric constant, containing linear loss and Kerr nonlinear effect. We make an approximation later, where the Kerr effect does not change the single mode shape and changes the eigenvalue in the first order approximation[24].

The nonlinear Schrödinger equation can be represented by a Hamiltonian matrix with a basis of single modes in individual waveguides with different spatial locations. $K_{i,j} = \left\langle F_i \left| \frac{1}{2\beta_0}\nabla_\perp^2 + \frac{k_0^2 n_0^2 - \beta_0^2 + 2\,k_0^2 n_0 n_2 |E|^2}{2\beta_0} \right| F_j \right\rangle$ and $E = \sum_i A_i |F_i\rangle|$, where i represents the index of the waveguides, $|F\rangle$ is a single mode and A_i is amplitude of fields for the ith waveguide. The nonlinear Schrödinger equation is represented using a matrix equation, $i\frac{\partial A_i}{\partial z} = -\widehat{K_{0ij}}A_j - \frac{k_0^2}{\beta_0} n_0 n_2 |A_i|^2 \delta_{i,j} A_j$, where $\widehat{K_0} = \frac{1}{2\beta_0}\nabla_\perp^2 + \frac{k_0^2 n_0^2 - \beta_0^2}{2\beta_0}$ is a linear operator and $\frac{k_0^2}{\beta_0} n_0 n_2 |A_i|^2 \delta_{i,j} A_j$ is the nonlinear operator with only diagonal terms. The transversal dimension derivative term could be removed by integrating the equation in transversal space owing to Gauss theorem. K_{ii}=0 when $\beta_0 = n_{eff} k_0$, where n_{eff} is the effective refractive index for a boundary mode at a specific frequency, ω_0. The off-diagonal terms, $K_{0,ij} = \frac{k_0^2}{2\beta_0}\left\langle F_i \left| n_0^2 \right| F_{j\neq i} \right\rangle$ are usually referred to as the coupling coefficient. In this case, only the nearest-neighbor coupling coefficients are considered, as the coupling coefficients between next-nearest waveguides are typically three orders of magnitude smaller than those between nearest neighbors. We take off the transversal dimension (xy) and $\beta(\omega) = \iint F^* n_0 k_0 F dxdy / \iint F^* F dxdy$, and apply a Taylor expansion on β_0 at a specific frequency ω_0. $\beta(\omega) = \beta_0 + \sum_m \frac{1}{m!}(\omega - \omega_0)^m \beta_m$

$$\frac{\partial A_i}{\partial z} = i\left(\beta(\omega) + \Delta\beta\right)\delta_{ij} A_j + \mathrm{iK}_{0,\mathrm{i}\neq\mathrm{j}} A_j$$

$$\Delta\beta = \iint F_i^* \Delta n k_0 F_i dxdy / \iint F_i^* F_i dxdy$$

Device fabrication and experimental characterization

The topological and trivial waveguides are fabricated using a 3 μm thermal oxide on silicon substrate as a starting point. 300 nm of ultra-silicon-rich nitride is deposited using chemical vapor deposition at a low temperature of 250 °C. The structures are patterned using electron-beam lithography and defined using reactive ion etching. To form the upper cladding of the devices, 2 μm of SiO_2 is deposited using chemical vapor deposition.

The temporal optical soliton experiments are performed using a mode-locked fiber laser at a 20 MHz repetition rate centered at 1550.1 nm. The optical power of the pulses is tracked using a power meter. The pulses are first adjusted for transverse electric polarization and coupled into and out of the devices using a tapered lensed fiber. Inverse taper couplers are used to terminate the devices. Characterization of the optical pulses is performed using an autocorrelator.

Data availability

The data that support the findings of this study are available from the corresponding authors upon reasonable request.

Received: 4 July 2024; Accepted: 7 November 2024
Published online: 14 November 2024

References

1. Haldane, F. & Raghu, S. Possible realization of directional optical waveguides in photonic crystals with broken time-reversal symmetry. *Phys. Rev. Lett.* **100**, 013904 (2008).
2. Wang, Z., Chong, Y., Joannopoulos, J. D. & Soljačić, M. Observation of unidirectional backscattering-immune topological electromagnetic states. *Nature* **461** (7265), 772–775 (2009).
3. Hafezi, M., Demler, E. A., Lukin, M. D. & Taylor, J. M. Robust optical delay lines with topological protection. *Nat. Phys.* **7** (11), 907–912 (2011).
4. Blanco-Redondo, A., Bell, B., Oren, D., Eggleton, B. J. & Segev, M. Topological protection of biphoton states. *Science* **362**, 568–571 (2018).
5. Wang, Y. et al. Topological protection of two-photon quantum correlation on a photonic chip. *Optica* **6**, 955–960 (2019).
6. Zhao, H. et al. Topological hybrid silicon microlasers. *Nat. Commun.* **9**, 1–6 (2018).
7. Bandres, M. A. et al. Topological insulator laser: experiments. *Science* **359**, 1–5 (2018).
8. Blanco-Redondo, A. et al. Topological optical waveguiding in silicon and the transition between topological and trivial defect states. *Phys. Rev. Lett.* **116**, 163901 (2016).

9. He, X. T. et al. A silicon-on-insulator slab for topological valley transport. *Nat. Commun.* **10**, 872 (2019).
10. Ma, J., Xi, X. & Sun, X. Topological photonic integrated circuits based on valley kink states. *Laser Photonics Rev.* **13**, 1900087 (2019).
11. Su, W. P., Schrieffer, J. & Heeger, A. J. Solitons in polyacetylene. *Phys. Rev. Lett.* **42**, 1698 (1979).
12. Meier, E. J., An, F. A. & Gadway, B. Observation of the topological soliton state in the Su-Schrieffer–Heeger model. *Nat. Commun.* **7**, 1–6 (2016).
13. Sohn, B. U. et al. A topological nonlinear parametric amplifier. *Nat. Commun.* **13** (1), 7218 (2022).
14. Leykam, D. & Chong, Y. D. Edge solitons in nonlinear-photonic topological insulators. *Phys. Rev. Lett.* **117**, 143901 (2016).
15. Mukherjee, S. & Rechtsman, M. C. Observation of Floquet solitons in a topological bandgap. *Science* **368**, 856–859 (2020).
16. Mittal, S., Moille, G., Srinivasan, K., Chembo, Y. K. & Hafezi, M. Topological frequency combs and nested temporal solitons. *Nat. Phys.* **17**, 1169–1176 (2021).
17. Wang, T. et al. Supercontinuum generation in bandgap engineered, back-end CMOS compatible silicon rich nitride waveguides. *Laser Photonics Rev.* **9**, 498–506 (2015).
18. Ng, D. K. T. et al. Exploring high refractive index silicon-rich nitride films by low-temperature inductively coupled plasma chemical vapor deposition and applications for integrated waveguides. *ACS Appl. Mater. Interfaces* **7**, 21884–21889 (2015).
19. Sohn, B. U., Choi, J. W., Ng, D. K. T. & Tan, D. T. H. Optical nonlinearities in ultra-silicon-rich nitride characterized using z-scan measurements. *Sci. Rep.* **9**, 1–7 (2019).
20. Choi, J. et al. Pure-quartic Bragg solitons in chip-scale nonlinear integrated circuits. *Optica* **10**, 1452–1460 (2023).
21. Choi, J. W. et al. Gap solitons on an integrated CMOS chip. *Nanophotonics* **12**, 1421–1433 (2023).
22. Sahin, E. et al. Bragg soliton compression and fission on CMOS-compatible ultra-silicon-rich nitride. *Laser Photonics Rev.* **13**, 1900114 (2019).
23. Choi, J. W., Sohn, B. U., Chen, G. F. R., Ng, D. K. T. & Tan, D. T. H. Soliton-effect optical pulse compression in CMOS-compatible ultra-silicon-rich nitride waveguides. *APL Photonics* **4**, 110804 (2019).
24. Agrawal, G. P. *Nonlinear Fiber Optics* (Academic, 1995).
25. Wang, M. et al. Topologically protected entangled photonic states. *Nanophotonics* **8**, 1327–1335 (2019).
26. Mollenauer, L. F., Stolen, R. H., Gordon, J. P. & Tomlinson, W. J. Extreme picosecond pulse narrowing by means of soliton effect in single-mode optical fibers. *Opt. Lett.* **8**, 289–291 (1983).
27. Eisenberg, H. S., Silberberg, Y., Morandotti, R., Boyd, A. R. & Aitchison, J. S. Discrete spatial optical solitons in waveguide arrays. *Phys. Rev. Lett.* **81**, 3383–3386 (1998).
28. Szameit, A. et al. Discrete nonlinear localization in femtosecond laser written waveguides in fused silica. *Opt. Express* **13**, 10552–10557 (2005).
29. Sohn, B. U. et al. Topologically protected parametric wavelength conversion in a valley hall insulator. *Laser Photonics Rev.* 2400045 (2024).
30. Fan, L. et al. An all-silicon passive optical diode. *Science* **335**, 447–450 (2012).
31. Zhang, Z. et al. Observation of edge solitons in photonic graphene. *Nat. Commun.* **11**, 1902 (2020).
32. Dobrykh, D. A., Yulin, A. V., Slobozhanyuk, A. P., Poddubny, A. N. & Kivshar, Y. S. Nonlinear control of electromagnetic topological edge states. *Phys. Rev. Lett.* **121**, 163901 (2018).
33. Smirnova, D., Leykam, D., Chong, Y. & Kivshar, Y. Nonlinear topological photonics. *Appl. Phys. Rev.* **7**, 021306 (2020).
34. Iwanow, R. et al. Observation of discrete quadratic solitons. *Phys. Rev. Lett.* **93**, 113902 (2004).
35. Fleischer, J. W., Carmon, T., Segev, M. & Efremidis, N. K. Christodoulides, D. N. Observation of discrete solitons in optically induced real time waveguide arrays. *Phys. Rev. Lett.* **90**, 023902 (2003).
36. Solnyshkov, D., Bleu, O., Teklu, B. & Malpuech, G. Chirality of topological gap solitons in bosonic dimer chains. *Phys. Rev. Lett.* **118**, 023901 (2017).
37. Lumer, Y., Rechtsman, M. C., Plotnik, Y. & Segev, M. Instability of bosonic topological edge states in the presence of interactions. *Phys. Rev. A* **94**, 021801 (2016).
38. Leykam, D. & Chong, Y. D. Edge solitons in nonlinear-photonic topological insulators. *Phys. Rev. Lett.* **117**, 143901 (2016).
39. Poddubny, A. N. & Smirnova, D. A. Ring dirac solitons in nonlinear topological systems. *Phys. Rev.* **98**, 013827 (2018).

Acknowledgements

Funding from the Ministry of Education ACRF Tier 2 Grant (T2EP50121-0019), Quantum Engineering Programme 2.0 grant (NRF2022-QEP2-01-P08), A*STAR MTC Grant (M21K2c0119), National Research Foundation Investigatorship (NRF-NRFI08-2022-0003) and A*STAR Institute of Microelectronics (C220415015) is gratefully acknowledged. The authors acknowledge processing and facilities under the National Research Foundation, Prime Minister's Office, Singapore, under its Medium Sized Centre Program, the Singapore University of Technology and Design, the UCSB Nanofabrication Facility, an open access laboratory, and the Agency for Science, Technology, and Research.

Author contributions

J. W. C. performed experimental characterization. D. K. T. N., J. S. G., G. F. R. C., H. G. and D. T. H. T. performed materials and device fabrication. J. W. C. and B. U. S. performed simulations. J. W. C., B. U. S. and D. T. H. T. analyzed the experimental data. J. W. C. wrote the manuscript with contributions from D. T. H. T. All authors contributed to the manuscript. D. T. H. T. supervised the project.

Declarations

Competing interests

The authors declare no competing interests.

Additional information

Correspondence and requests for materials should be addressed to D.T.H.T.

Reprints and permissions information is available at www.nature.com/reprints.

Publisher's note Springer Nature remains neutral with regard to jurisdictional claims in published maps and institutional affiliations.